Multi-axial 3D printing of biopolymer-based concrete composites in construction

Christ, Julian; Leusink, Sander; Koss, Holger

Published in:
Materials and Design

Link to article, DOI:
10.1016/j.matdes.2023.112410

Publication date:
2023

Document Version
Publisher's PDF, also known as Version of record

Materials & Design 235 (2023) 112410

Contents lists available at ScienceDirect

Materials & Design

journal homepage: www.elsevier.com/locate/matdes

Multi-axial 3D printing of biopolymer-based concrete composites in construction

Julian Christ *, Sander Leusink, Holger Koss

Technical University of Denmark, Brovej 118, 2800 Lyngby, Denmark

ARTICLE INFO

Keywords:
Biopolymer
3D printing
Concrete
Gelatin
Multi-axial printing

ABSTRACT

This paper explores the free-form potential of 3D concrete printing, enabled by a novel concrete-like composite made from 80 %-w/v mammal gelatin solution in water with 35 %-w/w gelatin solution to mineral aggregate ratio. This complete replacement of cementitious binders in 3D printing mortar aims on improving the sustainability and advancing the setting control through the material's thermoplasticity. The material was extruded with a novel and heated ram extruder, traversed with a KUKA robot arm, and cooled by a box fan under normal ambient temperature and humidity conditions. Printing trials with cylinders of 20 cm diameter and various overhang inclinations were carried out – both vertically and multi-directionally sliced. The overhang was increased until the fresh material could no longer support itself. The multi-directionally sliced objects showed the largest overhang capabilities. The thermoplastic printing mortar was able to print a maximum overhang of 80°. This demonstrated freedom of shape and applicability of the bio-based mortar to a 3D printing process could pave the way for highly optimized building components with a minimum use of material. This can incre the sustainability aspects of concrete structures.

1. Introduction

3D concrete printing has gained in popularity [1,2] and its industrial interest is increasing [3]. Numerous processes like powder bed printing [4] or mesh molding [5] were developed to produce digitally manufactured concrete structures. Especially extrusion-based 3D printing is commonly applied due to its large build volume and easy applicability to in-situ constructions [6]. The freedom to place material with extrusion processes and without the shape limitations of formwork allows the realization of architecturally advanced designs and material savings by constructing structurally optimized building components [7–10]. Furthermore, this new technology is expected to increase the construction industry's productivity by automation of processes [11]. The technology shows potential to lower the industry's environmental impact through material savings.

Constructing without formwork brings new challenges and sets high demands on the material's rheology. The material needs to be workable for extrusion and present high yield strengths right after deposition to support itself and further added layers under self-weight [12]. To enhance these properties, the current conventional material mixtures rely on a high share of cementitious material or injected accelerators to add to a fast yield stress development after extrusion [13,14]. The high percentage of cementitious materials is a particular drawback on the method's environmental performance [13]. A general lack of appropriate materials for 3D printing in constructions can be identified [6]. Recent studies aim on minimizing the used binder content by increasing the largest used aggregate size and enhance its rheological control [15], or improve the prediction of the material's structural capabilities to allow standardization [16]. Furthermore, other materials are being explored, including earth- and clay-based [17], polymeric-[18], geopolymer-[19,20], or bio-based filaments [21].

In earlier studies of the authors [22], a bio-based concrete composite was explored, which was made from the hydrogel mammal gelatin and sand. It showed good printable qualities through thermoplastic phase change. As shown in [22], such material made from sand and gelatin could increase its yield stress from 0.1 kPa to 106.1 kPa by cooling it from 50 °C to 20 °C. This translates to the printing temperature and ambient temperature condition respectively. By extruding and cooling under these conditions, a good buildability is expected. In comparison, cementitious filaments' early age stiffening show slower and weaker early age stress development [23] and commonly aim to reach a yield stress build-up of 1 kPa/min.

* Corresponding author.
E-mail address: julch@byg.dtu.dk (J. Christ).

https://doi.org/10.1016/j.matdes.2023.112410
Received 16 February 2023; Received in revised form 8 September 2023; Accepted 16 October 2023
Available online 17 October 2023

In cementitious materials, overhang geometries without the use of formwork in extrusion-based 3D concrete printing are, with some exceptions [9,14,24], therefore little explored or strongly limited. This leaves the lack of possible overhang geometry as a limiting factor for the realization of highly structurally optimized building components [9,10]. Gelatin-bound materials could increase the overhang capabilities of 3D concrete printing.

For small scale extrusion-based polymer desktop printers, overhang geometries are realized by printing support structures [25]. This is, due to the large additional material use, not pursued for up-scaled concrete printing. Some advanced slicing softwares showed a multi-directional slicing approach for smaller objects and printers. This can increase the support of the printed layer by inclining the preceeded layer, making separate support structures redundant [26–28]. Due to the low scale, the print bed, including the object itself, can easily be tilted in this process to avoid uneven deformation. On larger scales, this is not realizable. However, with robotic fabrication, 6-axis printing can produce multi-directionally printed objects without rotation of the printing bed [27,29]. The bio-based material, presented in [22], shows the potential to exhibit the necessary shape robustness to realize multi-axial prints without bed inclination and prevent deformation due to gravitational loading.

This paper presents a method and connected material mixture to produce advanced free-form construction with alternative concrete composites made from gelatin and sand. A material mixture showing sufficient buildability for overhang constructions is presented. A new connected printing methodology with a heated extruder and a 6-axis KUKA robot arm that can place the thermoplastic material is introduced. Furthermore, the slicing method to create a toolpath for the KUKA robot with a multi-directional slicing approach is presented. Finally, a comparison between vertically sliced and multi-directionally sliced objects is made to evaluate the maximum possible overhang and layer inclination for the biopolymer-based concrete. The respective failure mechanisms are being analyzed and discussed. The purpose of this research is to deliver a proof-of-concept for the developed process-material interaction. The obtained overhang structures and the description of the production process will give insights on build- and workability of the fresh material during the process, as well as the practicability of the operation and feasible manufacturing speed.

2. Materials

The bio-based concrete composite used for all samples consisted of a hydrogel binder from mammal gelatin and water, mixed with sand. In this study, gelatin replaced all conventionally used cementitious and mineral binders in 3D concrete printing applications. The mammal gelatin was purchased by the tool manufacturer DICTUM [30] (Art. Nr.: 450141) in granular form. Further specifications of the raw material can be found in [22].

Earlier studies [22] showed that mixtures of 80–120 %-w/v mammal gelatin solution in a 40 %-w/w hydrogel-aggregate ratio present the best printable results in terms of buildability and extrudability. As introduced, some of these mixtures showed a yield stress increase over 3 orders of magnitude during cooling from 50 °C to 20 °C. An 80 %-w/v mammal gelatin concentration was chosen for all tests to minimize binder content. Sand with a higher fine content than in earlier studies [22] was selected to increase thixotropic effects and ease printability. The alternation of sand made it necessary to adopt the hydrogel-aggregate ratio. Through print trials and by assessing the extrudability and buildability, the hydrogel-aggregate ratio was adopted to 35 %-w/w. Mix design example for the used mix: on 80 g of purchased mammal gelatin granulate, 100 g of water were added. These 180 g of hydrogel were prepared with 514 g of sand.

Sand with a specified maximum grain size of 0.18 mm was used. The sand was purchased as silica sand nr.13 from Dansand A/S. A corresponding grading curve can be seen in Fig. 1, which was experimentally determined after EN 933. The main mass of grains shows the size of 125–250 µm and the mass of fine particles (<63 µm) is about 5.01 %-wt. The sand had a moisture content of 0.1 %-wt. The light microscopy pictures in Fig. 2 show grains with sub-rounded to sub-granular geometrical properties.

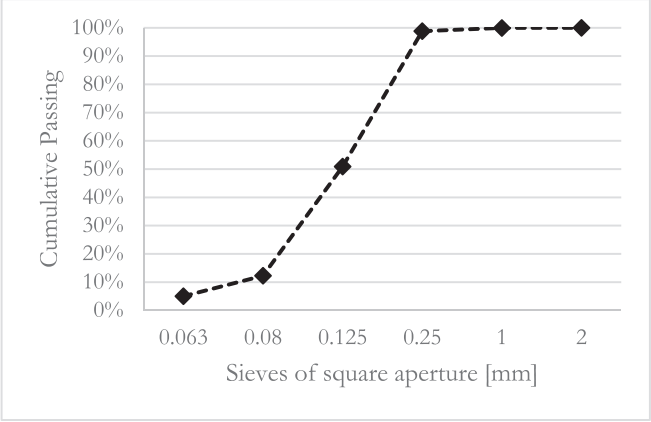

Fig. 1. Grain size distribution of silica sand.

3. Printing setup

3.1. Traversing mechanism

To move and control the position of the print head, a floor mounted KUKA robot KR2150 S C2 FLR ZH150/180″ of type KR150, produced in 2004 with a 150 kg payload was used (see Fig. 3). The robot was controlled by a KRC2 unit that uses the KUKA robot language (KRL) for programming.

In contrast to the three-axis gantry printers [29,31,32] for concrete applications, the six axes of the robot arm allows directly for rotation around all three axes. Therefore, a tilting of the extruder for controlling the print angle is possible. Other concrete robotic printers use this

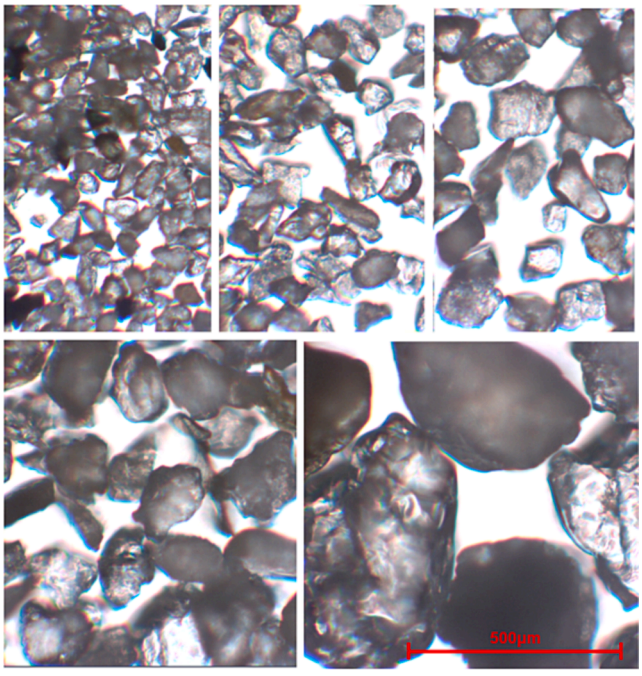

Fig. 2. Silica sand grain geometries of varying sizes, retained in sieves: (from top left to bottom right) Pan, 0.063 mm, 0.08 mm, 0.125 mm, 0.25 mm.

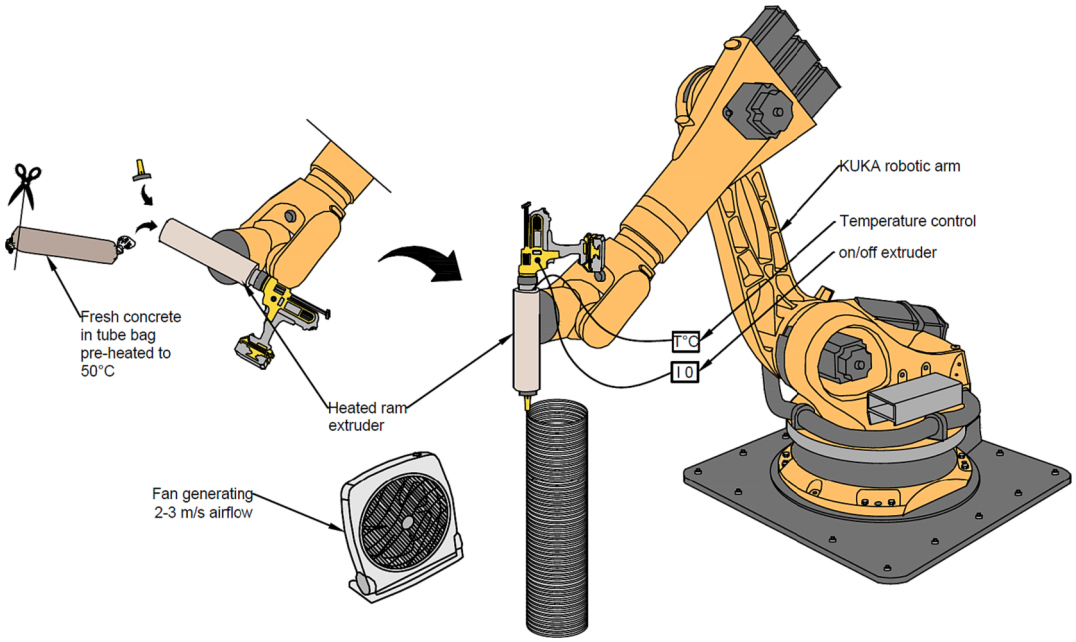

Fig. 3. Printing setup. The tubular bag with the pre-heated material was placed in the cartridge of the ram extruder. The extruder was held and moved by a KUKA robot arm. The temperature and extrusion could be controlled by external switches. After extrusion, the material was cooled by an airflow with a speed of 2–3 m/s created by a box fan.

additional freedom to reach difficult to access corners [33] or to incline the printed layer [14,34]. The six-axis controllability of the robot arm is necessary to test the proposed overhang constructions with layer inclination and prove this approach as an economical off-the-shelf traversing mechanism.

3.2. Extruder

A ram extrusion system similar to [35] and [36] was used. As described in [22], the ram extruder was adopted to elevate and keep the temperature of its filament. An automated caulking gun DEWALT DCE581E with a 600 ml capacity was used for this purpose. According to the manufacturer, the caulking gun puts pressure of 1.05 MPa [37] on its 5.5 cm diameter piston in an aluminum cartridge of 37 cm length. The standard speed of the piston is pre-defined at 40 mm/min but may vary due to changes in the resistance to the extrusion process. When filled, the sum of friction on the cylinder's inner walls was higher, hence slightly slowing down the extrusion speed. The material was forced through a nozzle with a cylindrical opening of 13 mm.

Fig. 4 shows a heating coil wrapped around the extrusion cylinder with a spacing of 1.5 cm and covered with an insulating foil and foamed rubber. A temperature switch was added to the heating coil and connected to a thermocouple, placed on the outside of the cartridge but underneath the insulation layer. The temperature of the aluminum cylinder could thereby be controlled and kept constant. Furthermore, an external on/off switch of the caulking gun was added to ease control. The nozzle was also insulated to prevent the material from cooling under standby time, potentially leading to clogging of the nozzle, and/or altering the extrusion's homogeneity (see Fig. 4).

3.3. Fan

A fan was used at a distance of about 50 cm to accelerate the cooling of the freshly printed layers. A 35 cm box fan from the producer MALMBERGS with the model number FB3501 was utilized. The fan flowrate was adjusted to create a constant airflow with a speed of 2–3 m/s around the sample. The air velocity was measured with a hand-held digital vane anemometer. The setup can be seen in Fig. 4.

3.4. Preheating of material

A UF160 oven from MEMMERT was used to preheat the material. At the temperature of 50 °C, the material was placed in the oven on a metal tray.

4. Methods

4.1. Material preparation

The binder was produced similar to earlier studies [22,38], using a Kenwood KCC9060S cooking chef machine. The machine is in general quite similar to mixers as widely used for manufacturing test specimens for cement and mortar testing [39] but allows additionally the control of heat input.

The mammal gelatin granulate was soaked in water for 30 min under low stirring and without heating in normal ambient room conditions. Subsequently, the material was heated under low stirring to 65 °C for 10 min. At this stage, the material proved to be nearly homogeneous and the granulate was fully dissolved. To produce the composite material, the binder was mixed with sand, pre-heated to 50 °C. Thereafter, the temperature and mechanical blending speed was kept unchanged for 20 min. The composite was then filled in tubular bags from low-density polyethylene with a wall thickness of 50 μm and a width of 80 mm. Closing both ends of the tubular bag with a simple knot prevented the material from drying during the preparation period. The material was stored in the tubular bags, holding around 500 ml of material, and under cooled conditions until printing preparation (see Fig. 3). The storing time was sufficiently brief to not allow degradation of the organic polymer and alteration of printing properties.

The material preparation was designed to avoid denaturing the polymer structure, creating a porous material, and preventing drying. Therefore, the material was not exposed to long heating periods, fast stirring, and storing the material outside closed containers for extended amount of time.

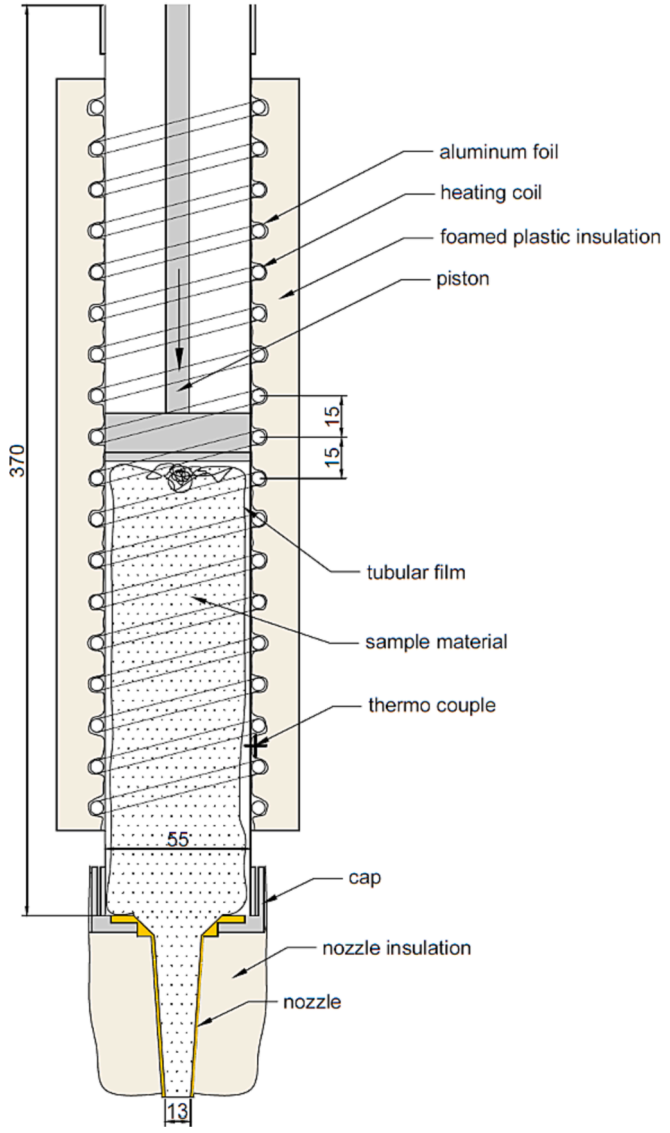

Fig. 4. Ram extruder design. An automated caulking gun DEWALT DCE581E was altered to be able to heat its cartridge with a heating coil and connected insulation. Measurements are given in [mm].
Adopted from [22]

4.2. Printing preparation

The extruder was pre-heated to 60 °C and kept at this temperature for another 30 min before filling the composite material bag. Simultaneously, the cool material bags were warmed in the oven to 50 °C. The materials were placed in the oven not longer than 2 h and at a minimum of one hour. This time frame aimed to ensure that the materials exhibited the same rheological properties and an even temperature profile between the batches. It could be observed that the material's porosity would decrease for more extended heating periods. The bags were kneaded for one minute before usage and after preheating to ensure a homogenous material at extrusion. The robot arm with the extruder was turned upwards for the refill (see Fig. 3). The warm bag was slid into the extruder, and the tip of the bag was cut off before reattaching the nozzle on the cartridge. The piston of the extruder was manually engaged, and the robot was brought in start position.

4.3. Printing

The extrusion speed from the 13 mm wide nozzle was kept constant at 10 mm/s (1.33 cm^3/s) and could be turned on/off manually with an external switch. The engagement of extrusion was timed with the manual onset of the robot arm movement. However, due to the material's elasticity and yield stress characteristic, the material extrusion showed some inertia in stopping and starting extrusion, especially when the cartridge was filled. Therefore, the extrusion was started slightly before the robot arm movement to enable a simultaneous onset of extrusion and movement.

Proper operation was controlled after each completed layer. The average printing time for a layer of a circular tube was about 40 s with an averaged extrusion or print head speed of 16 mm/s along the printing path. Time and speed varied for layers within the tube curvature to enable the creation of a varying layer thickness. The time between each layer, i.e., the rest time after completing the previous layer and starting the subsequent layer, was varied depending on the layer inclination and based on the rigidity assessment of the previous layer. The production time for each layer was estimated from 20 s time lapsed photographs.

The filling procedure of the cartridge gave an additional waiting time of 6–7 min after each 9th layer.

4.4. Multi-directional slicing and tool path calculation

A planar multi-directional slicing approach, similar to [40] was used to create a tool path. The slicing methodology was further edited and adjusted to the needs of the experimental setup:

1. For small scale polymer slicers, the print bed is usually rotated instead of the print head [27,28] to enable multi-directional printing – this is not feasible for extrusion-based 3D concrete printing since an on-site fabrication is envisaged.
2. The KUKA robot uses the manufacturer's own KUKA robotic language contrary to the conventionally used G-code language, i.e. the commands needed to be translated to this syntax.
3. The robot uses different location definitions for base and tool as well as for its coordinates, speed and acceleration.
4. Compared to desktop polymer printers, the extrusion rate of the used extruder could not be adjusted due to high inertial effects in the ram extrusion system. To enable the printing of layers with variable thicknesses, the extruded volume per unit length was controlled by its traversing speed.

A flow chart of the slicing methodology is seen in Fig. 5. The program incorporates the main steps of loading the model geometry, calculating a skeleton spline curve that serves as a normal vector to the slicing planes, generating a tool path. The tool path was created as G-code, and later translated to the Kuka-robot-language.

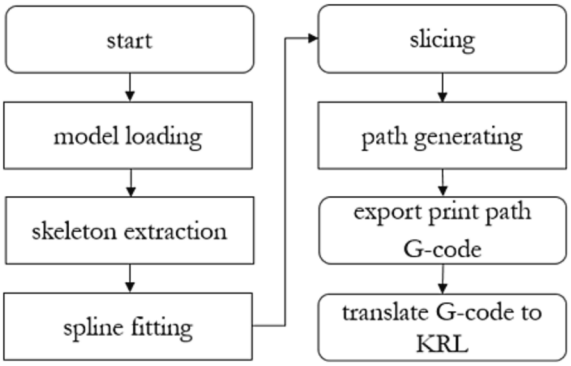

Fig. 5. Flow-chart of slicing algorithm.

4.4.1. Model loading

The models were prepared as Standard Triangle Language file (STL). The file contains a triangulated mesh, approximating the object (see Fig. 6 and Fig. 7), consisting of three vertices, defining a plane between them and, if required, the corresponding plane normal vector.

4.4.2. Skeleton extraction

The STL mesh was further abstracted to a skeleton line to identify a slicing curve representing the longitudinal direction of the object. Some approaches to calculate the skeleton line, such as the shape diameter function [42], mesh contraction method [43], and mean curvature flow method [44], were considered. Here, the method of [43] was used, providing itself as least computational demanding. The approach abstracts the mesh by contracting the object based on local curvature (see Fig. 7). The vertices of the model surface S are thereby moved in the direction of the local surface normal n by a distance Δp proportionate to the local curvature H. As in [44]:

$$\Delta p = Hn \tag{1}$$

This was done by using the discrete Laplacian equation of $LV^{'} = 0$, with V' being the vertex position and L being the *nxn* Laplace operator as described by Eq. (2) [43]:

$$L_{ij} = \begin{cases} \omega_{ij} = cot\alpha_{ij} + cot\beta_{ij} & if (i,j) \in E \\ \sum_{(i,k)\in E}^{k} - \omega_{ik} & if i = j \\ 0 & other \end{cases} \tag{2}$$

In which α_{ij} and β_{ij} are the opposite angles from the vertices i and j (see Fig. 6). To prevent the mesh contracting to a single point, the diagonal weighting matrices W_L and W_H are introduced according to [43], balancing the contraction and attraction, respectively:

$$\begin{bmatrix} W_L L \\ W_H \end{bmatrix} V^{'} = \begin{bmatrix} 0 \\ W_H V \end{bmatrix} \tag{3}$$

The contraction process is iterative and is performed after [43] by:

1. Solving the Laplacian equation $\begin{bmatrix} W_L^t L^t \\ W_H^t \end{bmatrix} V^{t+1} = \begin{bmatrix} 0 \\ W_H^t V^t \end{bmatrix}$ for the vertex position V^{t+1}.
2. Update the matrices $W_L^{t+1} = s_L W_L^t$ and $W_{H,i}^{t+1} = W_{H,i}^0 \sqrt{A_i^0 / A_i^t}$ where A_i^0 and A_i^t are the areas of the mesh ring around point i.
3. Calculate the Laplace operator L^{t+1} for step $t+1$ with Eq. (1)

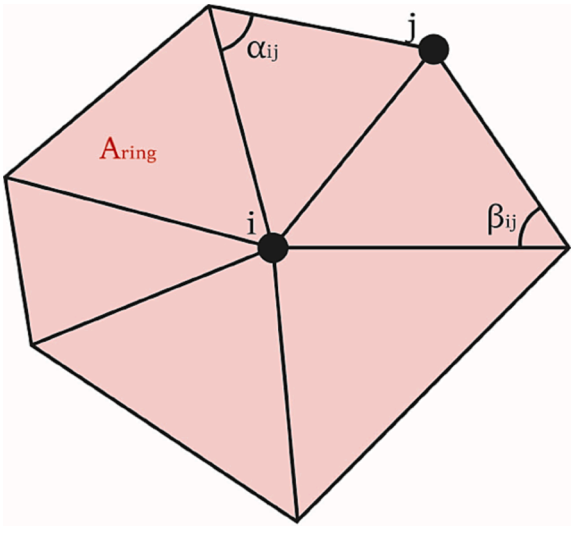

Fig. 6. Mesh cut-out with the vertices i and j and the opposite angles α_{ij} and β_{ij} of line $\overline{IJ}$ [41].

Similar parameters, as in [43], but slightly altered by trial and error were chosen to control the amount of detail in the contracted mesh: $W_H^0 = 1.0, W_H^0 = 10^{-2}\sqrt{A}$; $s_L = 2.0$; $\varepsilon = 5 \bullet 10^{-4}$. The contracted mesh was further processed from a contracted mesh to a point cloud of vertices (see Fig. 7). Terminating closures of 3D objects lead to deviations in the point cloud. Therefore, a margin of 5 % was removed at top and bottom of the curves.

4.4.3. Spline fitting

A 3rd order Bezier spline as in [40] was fit through the created point cloud to produce the final skeleton line. The spline was extrapolated beyond the end of the object to offset for the removed 5 % margin.

4.4.4. Slicing

The object was sliced into layers by dividing the skeleton spline into sections with the length of the layer thickness t_{layer}. The number of layers n_{layer} could be calculated by dividing the length of the spline $S(u)$ at a parametric distance u by t_{layer} [40]:

$$n_{layers} = \frac{S(u)}{t_{layer}} = \frac{1}{t_{layer}} \int_0^1 \sqrt{x'(u)^2 + y'(u)^2 + z'(u)^2} du \tag{4}$$

The slicing planes were defined at points along this curve, where S(u) is an integer multiple of the layer thickness.

$$S(u) = i \bullet t_{layer} \tag{5}$$

The corresponding normal vector of the slicing plane is S'(u). The printed thickness of the lines on the layers was calculated with the dynamic line thickness method as in [40].

The intersection of the slicing planes with the 3D surface is used to calculate the planar tool path, using conventional slicing methods [45]. Since the extrusion speed was fixed to a constant value, the extruded volume per millimeter printing track, i.e. the layer thickness, was controlled by adjusting the print speed (see appended video appended) with:

$$v = \frac{Q}{t_L \bullet w_L} \tag{6}$$

Where Q is the flow rate of the nozzle, t_L is the local layer thickness and w_L is the layer width. Since Q and w_L are constant, Q/w_L can be seen as a factor.

4.4.5. Export

The printing path was exported to G-code to allow an ubiquitous export format for computer numerical controlled machining. The printing path was noted as a G1 movement for constant speed, while all other relocation motions were denoted as G0 for faster movements.

The G-code could then be translated to the KRL syntax by using the correlations stated in Table 1. Most parameters can directly be correlated. However, some values, such as speed and acceleration, require additional lines in KUKA-robot-language and therefore need special translation. Also, units differed from G-code to KRL and needed to be adjusted. The tool and base definition was done manually with the KUKA robot's built-in software.

The implemented *slicing-* and *G-code to KRL translation algorithm* that was used in this paper can be found in [41].

4.5. Printed geometries

To test the maximum overhangs that can be produced with the bio-

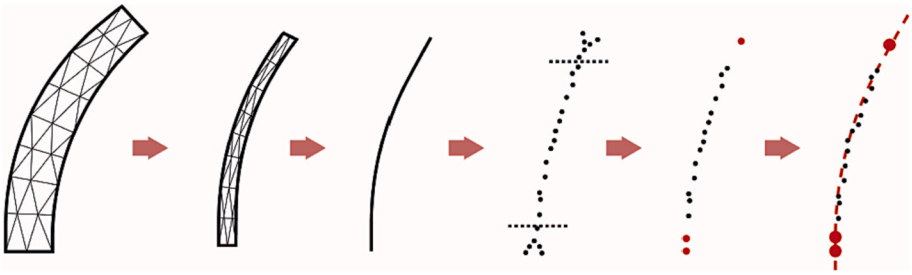

Fig. 7. Skeleton line calculation. The mesh of the STL file is being contracted to a point cloud, trimmed and approximated by a spline curve [41].

Table 1
Conversion from G-code to KUKA. The Section 'common commands' show directly convertible values between the G-code and KRL syntax. Underneath, the Kuka specific variable are specified which do not have a value in G-code.

		G-code	KRL
common commands	Coordinate (cdnt)	X.. Y.. Z.. A.. B.. C..	{X.., Y.., Z.., A.., B.., C..}
	Tool Selection	T..	$TOOL = TOOL_DATA[..]
	Base Selection	G92 X.. Y.. Z..	$BASE = BASE_DATA[..]
	Rapid motion	G0 [cdnt]	PTP[cdnt]
	Controlled linear mot.	G1 [cdnt]	LIN[cdnt]
	Controlled circular mot.	G2 [cdnt] I.. J..	CIRC[cdnt], [cdnt]
		G3 [cdnt] I.. J..	CIRC[cdnt], [cdnt]
	Home all axis'	G28	PTP HOME
	Velocity	F..	$VEL.CP =..
	Acceleration	M204 S..	$ACC.CP =..
	Initialize	G21; G90; G92 E0;	INI
	Pause	M1	HALT
	Comments	;	:
Add. KRL commands	Approximate linear mot.		[lin motion] C_DIS
	Approximate distance		$APO.CDIS =..
	Orientation control		$ORI_TYPE #..

based composite material in vertical and the multi-directional slicing, eight shapes were defined (see Fig. 8). To simplify the test of the concept, a circular cross-section was chosen with a diameter of 20 cm. Inclinations of 10°, 20°, 30°, 40°, 50°, 60°, 70° and 80° were defined to identify the limit for material and printing method. The average layer height was defined as 5 mm (see Fig. 9). The layer width resulted, as discussed before, from the defined extrusion-, printing speed, nozzle size, and layer height in 13–15 mm (see Fig. 9).

Naturally, if a layer thickness shall be larger than zero at any point, the change of inclination between two successive layers, or the curvature of skeleton is limited. Fig. 10 shows the geometry for a multi-axial 3D printing approach. The inner layers, closest to the center of rotation should not lay beneath a certain thresh-hold to enable a good print quality. In the case of this study, the thresh hold was chosen to be ± 2 mm respective to the average layer thickness. A general formulation for the minimum rotation radius for this boundary condition could be derived of the geometrical circumstances in Fig. 10.

This can be seen in Eq. (7):

$$\min r = \frac{R + 0.5w}{x} \tag{7}$$

With: r - radius of pipe's curvature from rotational center to center of cross-section$R$ - radius of circular pipe's cross-section centerw - layer widthx - possible variance of layer (printability boundary); layer height $H \pm xH$; $0 \leq x \leq 1$

For the layer thickness, a variation factor of $x = 2/5$ was defined, i.e. the standard layer height of $H = 5mm$ was varied by: $\pm xH = \pm\frac{2}{5} \bullet 5mm = \pm 2mm$. The minimum radius of the cylinders was calculated as $minr = 269mm$.

It was expected to be able to print larger overhang geometries with the multi axes slicing direction, rather than the standard vertical build directions as known from other projects [9,24]. Therefore, the prints were started out with a vertical build direction, horizontal slicing, and a low overhang. The overhang was increased for each print, up to the point of observable failure in the manufacturing. To push beyond this point, the slicing methodology was switched to the multi axial slicing approach and continued to the maximum overhang/inclination of 80° (see Fig. 8).

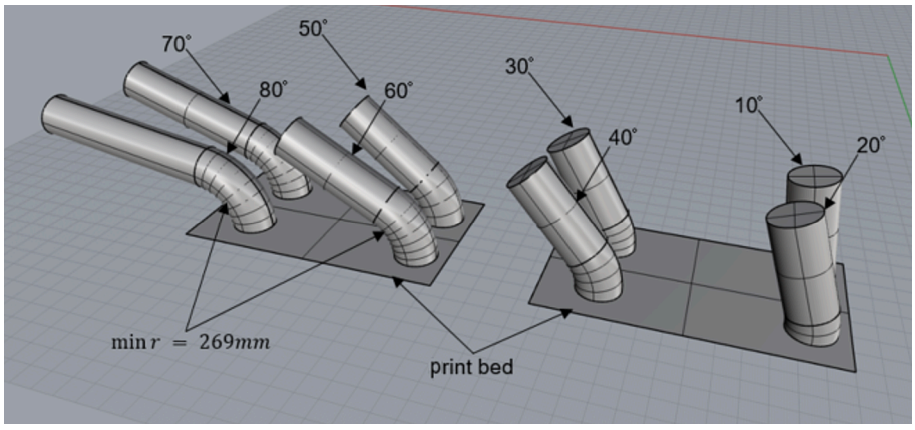

Fig. 8. Modelled printing objects in Rhinoceros 6. Cylinders with an inclination of 10°-80° and a cylindrical cross section with a diameter of 20 cm. The minimum radius of the rotation was calculated after Eq. (7). Four objects were fitted on the dimension of the printing bed.

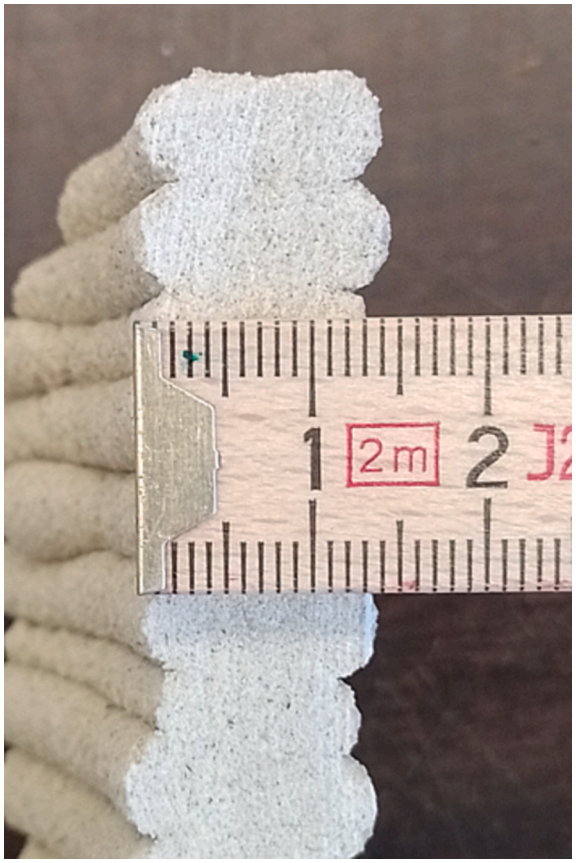

Fig. 9. Vertical cross-section of 80° inclination as seen in Fig. 8. The layer width of 13–15 mm and a layer height of approx. 5 mm is identifiable.

5. Results and discussion

5.1. Printing cylinders

The printed elements are shown in Fig. 11. The top row shows the cylinders that were sliced with a vertical build direction – a maximum of 40-50° could be reached. The second row shows the multi-directionally sliced cylinders, for which a significantly higher layer inclination of 80° could be achieved.

The 50° overhang of the vertically sliced element was not printable. The areas of the layers that present the largest overhang (see bottom left of Fig. 11) showed deformation during the print and later failure. In the regions of outmost lateral offset, the layer geometries lacked support and could therefore not be pressed onto the preceeded layer by the tip of the nozzle, thus keeping its cylindrical shape. The connection of the printed layer was insufficient to keep the material in place; it deformed and fell down. The identified printability limit in overhang originated from the material's loss of equilibrium and thus the lack of connection. To avoid this issue, small-scale polymer printers incorporate a temporary support structure that needs to be removed after completion of the print [25]. This is due to practical reasons not feasible for concrete printing, leaving to reach larger overhangs to increase the tack (adhesion strength of printed layers), normal strength, and yield stress of the material, or creating increased support by layer inclination as explored in this study and shown in Fig. 11.

An overhang of 50° could be reached without any further complications with the multi-axial printed objects, suggesting that the increased layer inclination gives better buildability for overhang constructions. The overhang inclination was increased to 80°. The material showed at the reached inclination still good buildability without significant deformation. A failure occurred in the location of high tensile stresses normal to the layer interface plane due to a large moment induced by self-weight of the cantilevering arch of the curved tube (see bottom right of Fig. 11). Even though a failure was observed, the local deposition of the layer under an 80° inclination was still sufficient to meet the occurring tensile and shear stresses. The structural failure at 80° could be avoided by choosing a greater layer time to give the material a longer hardening time before being loaded.

The introduction of cold joints might be the reason for the failure at the given location (see Fig. 11). When reloading the ram extruder, the deposited material cooled down. The introduced warmer layer might lacked adhesion due to the temperature difference. This needs to be further investigated in future studies. However, the binder gelatin, also known as bone glue, is recognized for its good self-adhesion in cabinet making applications. I.e. already glued joints can be repaired by simply adding more glue. Good interface adhesion and little cold joint effects are therefore expectable.

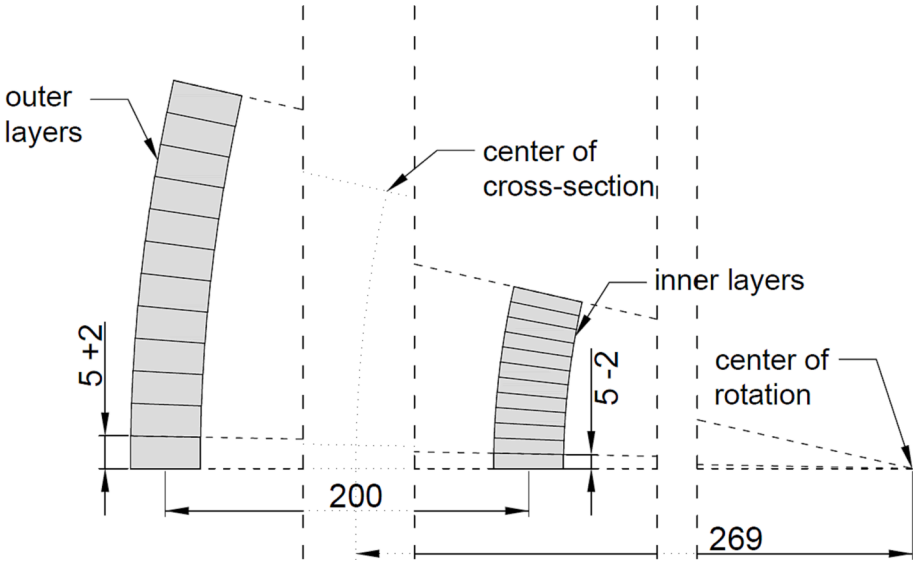

Fig. 10. Geometrical limits for rotation radius with a layer height variance of ± 2 mm. All measurements are given in [mm]. The layers, laying on the inside of the rotation can be 2 mm decreased, the layers on the outside can be 2 mm increased, related to the chosen layer height of 5 mm. Eq. (7) shows the calculation of the minimum radius of 269 mm to satisfy those limits.

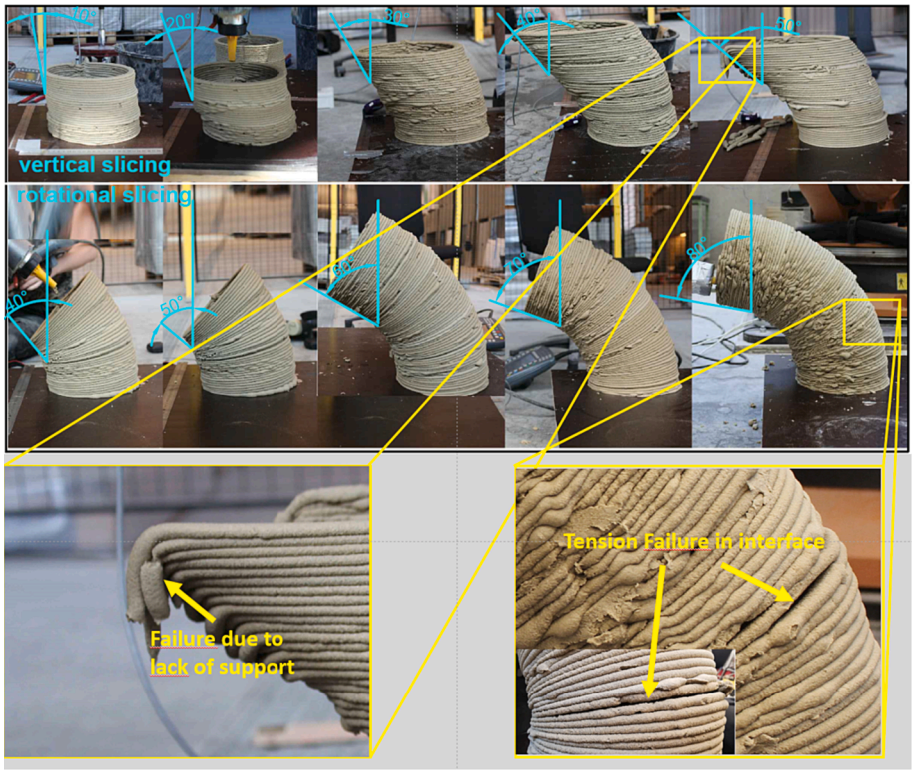

Fig. 11. Prints of varying overhang geometry. Cross-section of pipe kept constantly circular with diameter of 20 cm. Increasing overhang from 10° (top left) to 80° bottom right. Built with varying slicing strategies: vertical slicing (top) and rotational slicing (middle). 40° inclination was the largest inclination possible for vertical slicing methods, for rotational slicing, 80° inclination was achieved. Mechanisms of the respective failures can be seen in the bottom of this figure.

The layer times were chosen, as seen in Fig. 12. For close to vertical build-up without overhang, a continuous print was conducted without any resting time between the layers, i.e., the layer time matched the time for the nozzle to print one layer – 40 s, as described in Section 4.3. As the built inclination increased, a more significant yield strength increase was needed to keep the material in place. As described in [22], the yield stress and stiffness of the material increase when given time to settle (thixotropy) and by cooling the material. Therefore, the increase of the layer time could add to the obtainable layer stability. A continuation of a 40 s layer time would have led to an earlier collapse of the overhang

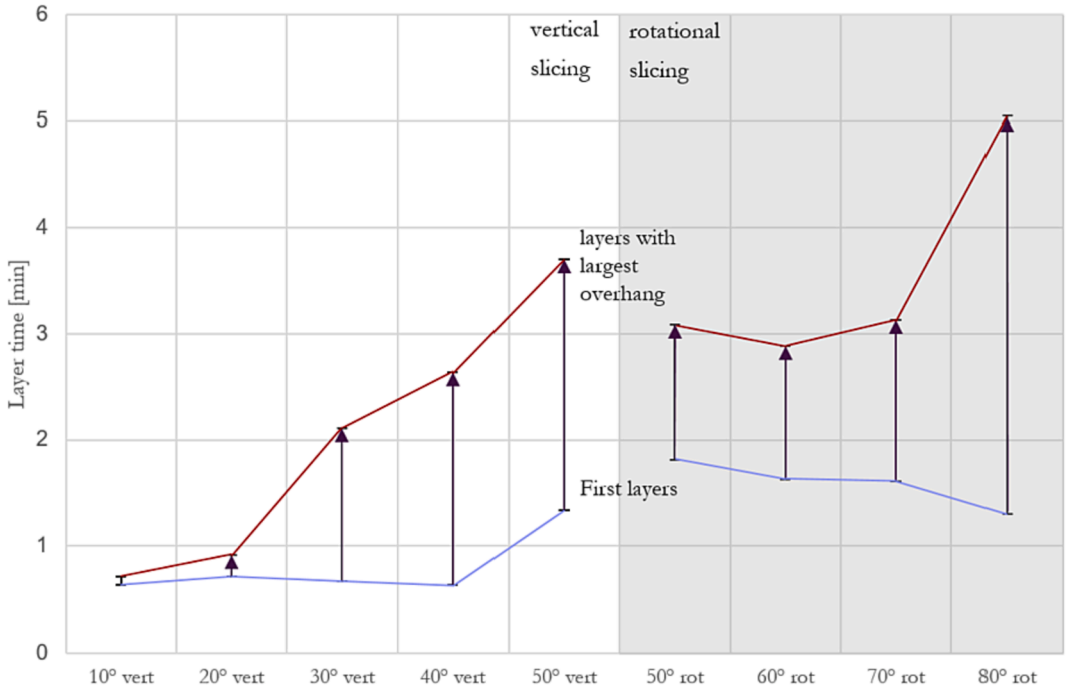

Fig. 12. Mean layer time for (left) vertically sliced objects, (right) for multi-directionally sliced objects. The mean is taken over approx. 9 layers or each cartridge of the caulking gun.

structures. The layer times were increased in regards to the layer inclination. The average layer time did not exceed 5 min for reasons of manufacturing practicability.

Similar studies were attempted to reach a high inclination of overhang with vertical build direction methodologies for polymer printers [46] and cementitious concrete printers [9,24]. In [24], a maximum overhang in the vertical direction of 17.5° could be reached by optimizing the composition of cementitious material with the addition of fly ash. Similar results to this study give limits of polymer printers which are communicated with approx. 45° [47]. Depending on the layer thickness, a limit of 45° is often noted as a theoretical limit for a vertically sliced object [46]. Since the layer width matches the layer's height, 50 % of the deposited material lacks support, giving equilibrium issues of the supported layer, without relying on the materials tack.

Also in concrete printing, significant overhangs can be reached by either increasing the layer width or inclining the layers [34,48]. For inclined layers, larger overhangs than 17.5° can be achieved [48]. However, the material's buildability is still limited, i.e., the rather slow setting characteristics are the limiting factor. For the presented concrete composite, a fast setting time through thermoplastic hardening can be reached and, therefore, high layer inclinations compared to conventional concrete composites. The high density and mass of the material also limits the overhang constructions due to the induced moment, not being able to reach as high overhangs as for other, less dense materials, such as plastics.

5.2. 6-axis printing

The robot arm allowed a 6-axes control, i.e., movement along 3 axis and adjustment of yaw and pitch angles of the print head. Therefore, the extrusion system could be placed normal to the layer plane for all slicing direction hence optimizing the material deposition. A limiting factor is the size of the print head, which could for complex geometries and small operation space collide with the already existing part of the structure. If not solved otherwise through advanced print head design, the print inclination would need to be limited for larger overhangs or limited printing spaces to give the print head enough room without damaging already printed parts. Similar processes can be seen in [33,48].

The sliced planes were printable both for the vertical and multi-directional printing approach. The layers of the conventional slicer showed, as expected, a uniform layer height, while the layer height of the multi-directional sliced pipes varied. The allowed variation of the layer thickness of $\pm 2mm$ as determined in Section 4.5, was for some layers exceeded or undercut but without damaging the proceeding layer (see Fig. 11). The intended maximum variation was exceeded. It can therefore be concluded that the calculated skeleton line and the centerline of the circular cross-section are similarly placed but not alike.

5.3. Extrusion and material

The extrusion through a caulking gun with preheated material as seen in Fig. 4, was a simple but effective design successfully applied for building the geometries intended. The material showed good homogeneity at extrusion. The material's consistency could vary slightly from batch to batch depending on pre-heating duration. This consistency change originates from mixing variations and the vapor permeability of the low density polyethylene film tube bags. During the heating period, the water content in the material is being decreased. In addition, the material is given time to settle while being heated and air enclosures in the material from the mixing process are being driven to the surface. The volume of solid material in the tube bag could therefore decrease through segregation in the solid- and gas phase, leaving the solid phase with varying consistencies. This variation, lead to difficulties in controlling the onset of the ram extruder. Thicker materials needed more built-up pressure in the extruder and therefore an earlier onset of the piston. The print quality varied therefore. An improvement of print quality could in future be reached by introducing an auger to the nozzle, in order to more effectively control material extrusion.

The printability of the material is proofed to show sufficient robustness for large layer inclinations. No tearing was observed from the deformation, and no plastic deformation due to self-weight was observed. The filament could be deformed from a cylinder shape of 13 mm diameter to a layer with a height of 5 mm through nozzle placement and movement.

The freedom-of-shape that is possible with the material and process makes the application to constructions plausible. However, the main limiting factor for the application is the durability of the material. Fire- and moisture resistance and protection against micro-organisms need to be investigated and further developed. To the current state, the printed objects take up moisture from humid environments. If sufficient free water is available within the composite, it gives room for growth of micro-organisms. Further, the printing mechanism is to date limited to a ram extrusion system. To increase its practicability, a continuous printing system should be developed that can deliver the material in a more effective way to the nozzle, e.g. through pumping.

6. Conclusion

The process and the related material to print structures with large overhangs were presented. It was shown that with a multi-directional planar slicing methodology larger overhang structures could be reached than with the conventionally used vertical build direction methods. The multi-directional slicing approach, for which a skeleton line presents the slicing normal, offered better support for the freshly printed layers and could therefore enable higher degrees of freedom. The biopolymer-based thermoplastic concrete composite material developed early-age properties that showed sufficient rigidity to hold a freshly printed layer in place - also under 80° layer inclination. The heated ram extruder could keep the preheated composite material at temperature and allow for homogeneous extrusion with a rapid early-age yield stress development.

The improvement of rheological properties are decreasing the overhang limitations for 3D printed construction materials. With larger overhangs, higher degrees of structural optimization in building components and therefore a lower material consumption are possible. This paper could show that freedom of shape and large overhangs can be enabled by thermoplastic substitutes for conventional binders in concretes like the presented mammal gelatin.

Declaration of Competing Interest

The authors declare that they have no known competing financial interests or personal relationships that could have appeared to influence the work reported in this paper.

Data availability

Data will be made available on request.

Acknowledgements

This research was funded by the Department for Civil Engineering at the Technical University of Denmark and the VILLUM FONDEN (grant nr. 00023307).

Appendix A. Supplementary data

Supplementary data to this article can be found online at https://doi.org/10.1016/j.matdes.2023.112410.

References

[1] R.A. Buswell, W.R. Leal de Silva, S.Z. Jones, J. Dirrenberger, 3D printing using concrete extrusion: A roadmap for research, Cem. Concr. Res. 112 (2018) 37–49.
[2] F. Lyu, D. Zhao, X. Hou, L. Sun, Q. Zhang, Overview of the Development of 3D-Printing Concrete: A Review, Appl. Sci. 11 (2021) 9822.
[3] A. Siddika, M.A.A. Mamun, W. Ferdous, A.K. Saha, R. Alyousef, 3D-printed concrete: applications, performance, and challenges, J. Sustain. Cem. Mater. 9 (2020) 127–164.
[4] D. Lowke, E. Dini, A. Perrot, D. Weger, C. Gehlen, B. Dillenburger, Particle-bed 3D printing in concrete construction - Possibilities and challenges, Cem. Concr. Res. 112 (2018) 50–65.
[5] N. Hack, W.V. Lauer, Mesh-mould: Robotically fabricate spatial meshes as reinforced concrete formwork, Archit. Des. 84 (2014) 224–231.
[6] D. Mierzwinski, M. Lach, S. Gqdek, W.-T. Lin, D.H. Tran, K. Korniejenko, A brief overview of the use of additive maufacturing of concreate materials in construction, Acta Innov. 48 (2023) 22–37.
[7] J. Liu, V. Nguyen-Van, B. Panda, K. Fox, A. Du Plessis, P. Tran, Additive Manufacturing of Sustainable Construction Materials and Form-finding Structures: A Review on Recent Progresses. 3D Print, Addit. Manuf. 9 (2022) 12–34.
[8] Y.W.D. Tay, J.H. Lim, M. Li, M.J. Tan, Creating functionally graded concrete materials with varying 3D printing parameters, Virtual Phys. Prototyp. 17 (2022) 662–681.
[9] G. Vantyghem, W. De Corte, E. Shakour, O. Amir, 3D printing of a post-tensioned concrete girder designed by topology optimization, Autom. Constr. 112 (2020), 103084.
[10] G.D. Schutter, K. Lesage, V. Mechtcherine, V.N. Nerella, G. Habert, I. Augusti-Juan, Vision of 3D printing with concrete - Technical, economic and environmental potentials, Cem. Concr. Res. 112 (2018) 25–36.
[11] WEF, W.E.F., 2016. Shaping the Future of Construction A Breakthrough in Mindset and Technology, Industry Agenda.
[12] N. Roussel, Rheological requirements for printable concretes, Cem. Concr. Res. 112 (2018) 76–85.
[13] T. Wangler, N. Roussel, F.P. Bos, T.A.M. Salet, R.J. Flatt, Digital Concrete: A Review, Cem. Concr. Res. 123 (2019).
[14] C. Gosselin, R. Duballet, P. Roux, N. Gaudillière, J. Dirrenberger, P. Morel, Large-scale 3D printing of ultra-high performance concrete - a new processing route for architects and builders, Mater. Des. 100 (2016) 102–109.
[15] W.R. Leal da Silva, M. Kaasgaard, T.J. Andersen, Sustainable 3D Concrete Printing with Large Aggregates, in: Digital Concrete 2022, Loughborough, United Kingdom, 2022, pp. 71–77.
[16] C. Richter, J. Jungwirth, 3D Concrete Printing - from Mechanical Properties to Structural Analysis, in: Digital Concrete 2022, Loughborough, United Kingdom, 2022, pp. 201–210.
[17] M. Gomaa, W. Jabi, V. Soebarto, Y.M. Xie, Digital manufacturing for earth construction: A critical review, J. Clean. Prod. 338 (2022), 130630.
[18] M.H. Ali, G. Issayev, E. Shehab, S. Sarfraz, A critical review of 3D printing and digital manufacturing in construction engineering, Rapid Prototyp. J. (2022).
[19] B. Panda, C. Unluer, M.J. Tan, Investigation of the rheology and strength of geopolymer mixtures for extrusion-based 3D printing, Cem. Concr. Compos. 94 (2018) 307–314.
[20] J.H. Lim, B. Panda, Q.C. Pham, Improving flexural characteristics of 3D printed geopolymer composites with in-process steel cable reinforcement, Constr. Build. Mater. 178 (2018) 32–41.
[21] M. Sinka, J. Zorica, D. Bajare, G. Sahmenko, A. Korjakins, Fast setting binders for application in 3d printing of bio-based building materials, Sustain. 12 (2020) 1–12.
[22] Christ, J., Perrot, A., Ottosen, L.M., Koss, H., 2023. Rheological characterization of temperature-sensitive biopolymer-bound 3D printing concrete. Submitted to Construction and Building Materials.
[23] R. Jayathilakage, P. Rajeev, J. Sanjayan, Yield stress criteria to assess the buildability of 3D concrete printing, Constr. Build. Mater. 240 (2020), 117989.
[24] F. Brun, F. Gaspar, A. Mateus, J. Vitorino, F. Diz, Experimental Study on 3D Printing of Concrete with Overhangs, RILEM Bookseries 28 (2020) 778–789.
[25] S.C. Ligon, R. Liska, J. Stampfl, M. Gurr, R. Mülhaupt, Polymers for 3D Printing and Customized Additive Manufacturing, Chem. Rev. 117 (2017) 10212–10290.
[26] P. Singh, D. Dutta, Multi-direction slicing for layered manufacturing, J. Comput. Inf. Sci. Eng. 1 (2001) 129–142.
[27] C. Dai, C.C.L. Wang, C. Wu, S. Lefebvre, G. Fang, Y.J. Liu, Support-free volume printing by multi-axis motion, ACM Trans. Graph. 37 (2018).
[28] X. Wang, L. Chen, T.Y. Lau, K. Tang, A skeleton-based process planning framework for support-free 3+2-axis printing of multi-branch freeform parts, Int. J. Adv. Manuf. Technol. 110 (2020) 327–350.
[29] X. Cao, S. Yu, H. Cui, Z. Li, 3D printing devices and reinforcing techniques for extruded cement-based materials: a review, Buildings 12 (2022) 1–19.
[30] DICTUM, 2019. More than Tools - Dictum [WWW Document]. URL https://www.dictum.com/en/ (accessed Apr.23rd 2019).
[31] A.V. Rahul, M. Santhanam, Evaluating the printability of concretes containing lightweight coarse aggregates, Cem. Concr. Compos. 109 (2020), 103570.
[32] F. Bos, R. Wolfs, Z. Ahmed, T. Salet, Additive manufacturing of concrete in construction: potentials and challenges of 3D concrete printing, Virtual Phys. Prototyp. 11 (2016) 209–225.
[33] XTree, 2019. 3D Printed Wall with integrated window frame [WWW Document]. Youtube video. URL https://www.youtube.com/watch?v=0byQtXW5Gm8 (accessed Jul. 18th 2022).
[34] Dressler, I., Freund, N., Lowke, D., 2020. The effect of accelerator dosage on fresh concrete properties and on interlayer strength in shotcrete 3D printing. Materials (Basel). 13.
[35] D.G. Soltan, V.C. Li, A self-reinforced cementitious composite for building-scale 3D printing, Cem. Concr. Compos. 90 (2018) 1–13.
[36] P. Shakor, S. Nejadi, G. Paul, A study into the effect of different nozzles shapes and fibre-reinforcement in 3D printed mortar, Materials (basel) 12 (2019).
[37] DeWALT, 2018. 18V XR Fugepistol med holder til patron, løs enhed [WWW Document]. URL https://www.dewalt.dk/powertools/productdetails/catno/DCE581N/ (accessed Jul.18th 2022).
[38] Christ, J., Koss, H., Ottosen, L.M., 2019. A concrete composite from biologically based binders and mineral aggregates for constructional 3D-printing. In: 2nd International Conference of Sustainable Building Materials. Eindhoven, The Netherlands.
[39] Dansk Standard, 2016. DS/EN 196-1:2016 Metoder til prøvning af cement – Del 1 : Styrkebestemmelse Methods of testing cement – Part 1 : Determination of strength.
[40] M. Wang, H. Zhang, Q. Hu, D. Liu, H. Lammer, Research and implementation of a non-supporting 3D printing method based on 5-axis dynamic slice algorithm, Rob. Comput. Integr. Manuf. 57 (2019) 496–505.
[41] Leusink, S., 2020. Development of a slicing and control application for construction - scale 3D printing with polymeric concrete composites. Master Thesis. Technical University of Denmark.
[42] L. Shapira, A. Shamir, D. Cohen-Or, Consistent mesh partitioning and skeletonisation using the shape diameter function, Vis. Comput. 24 (2008) 249–259.
[43] O.K.C. Au, C.L. Tai, H.K. Chu, D. Cohen-Or, T.Y. Lee, Skeleton extraction by mesh contraction, ACM Trans. Graph. 27 (2008) 1–10.
[44] A. Tagliasacchi, I. Alhashim, M. Olson, H. Zhang, Mean curvature skeletons, Eurographics Symp. Geom. Process. 31 (2012) 1735–1744.
[45] S.H. Choi, K.T. Kwok, A tolerant slicing algorithm for layered manufacturing, Rapid Prototyp. J. 8 (2002) 161–179.
[46] Y. Mass, O. Amir, Topology optimization for additive manufacturing: Accounting for overhang limitations using a virtual skeleton, Addit. Manuf. 18 (2017) 58–73.
[47] F. Wulle, D. Coupek, F. Schäffner, A. Verl, F. Oberhofer, T. Maier, Workpiece and machine design in additive manufacturing for multi-axis fused deposition modeling, Proc. CIRP 60 (2017) 229–234.
[48] Twente, 2020. 3D Printing Concrete Live - World's Records (Time Lapse) [WWW Document]. Youtube video. URL https://www.youtube.com/watch?v=uCE0ojKWqSM (accessed Jul.19th 2022).